Semi-transparent, flexible, and electrically conductive silicon mesh by capillarity-driven welding of vapor-liquid-solid-grown nanowires over large areas

Thomas A. Celano, Seokhyoung Kim, David J. Hill, and James F. Cahoon (✉)

Department of Chemistry, University of North Carolina at Chapel Hill, Chapel Hill, NC 27599-3290, USA

ABSTRACT

Bottom-up synthesis of semiconductor nanowires (NWs) by the vapor-liquid-solid (VLS) mechanism has enabled diverse technological applications for these nanomaterials. Unlike metallic NWs, however, it has been challenging to form large-area interconnected NW networks. Here, we generate centimeter-scale meshes of mechanically and electrically interconnected Si NWs by sequentially growing, collapsing, and joining the NWs using a capillarity-driven welding mechanism. We fabricate meshes from VLS-grown NWs ranging in diameter from 20 to 100 nm and find that the meshes are three-dimensional with a thickness ranging from ~ 1 to ~ 10 microns depending on the NW diameter. Optical extinction measurements reveal that the networks are semi-transparent with a color that depends on the absorption and scattering characteristics of individual NWs. Moreover, active voltage contrast imaging of both centimeter- and micron-scale meshes reveals widespread electrical connectivity. Using a sacrificial layer, we demonstrate that the mesh can be liberated from the growth substrate, yielding a highly flexible and transparent film. Electrical transport measurements both on the growth substrate and on liberated, flexible films reveal electrical conduction across a centimeter scale with a sheet resistance of ~ 160–180 kΩ/square that does not change significantly upon bending. Given the ability to encode complex functionality in semiconductor NWs through the VLS process, we believe these meshes of networked NWs could find application as neuromorphic memory, electrode scaffolds, and bioelectronic interfaces.

KEYWORDS

semiconductor nanowire, conductive network, flexible electronics, welding, thermal annealing, active-voltage contrast

1   Introduction

The bottom-up growth of semiconductor nanowires (NWs) provides the opportunity to encode diverse properties for a range of electronic, photonic, and bioelectronic applications [1, 2], yet integrating large numbers of NWs into functional devices represents a substantial challenge. Some applications require the precise positioning and alignment of single NWs [3], but other applications may be able to utilize disordered or semi-disordered networks or ensembles of NWs. For instance, relatively disordered Si NWs have already been used as battery electrodes [4], sensors in artificial skin [5], and scaffolds for graphene [6]. Similarly, for carbon nanotubes [7], and especially metallic NWs [8–11], disordered networks have found widespread application as transparent thin-film conductors, where the NWs or nanotubes are often dispersed from solution onto substrates and annealed to produce conductive percolation pathways through a quasi-two-dimensional thin-film network. The films exhibit high flexibility, transparency, and inter-connectivity. These same qualities could be advantageous in a semiconductor network designed for biological, photovoltaic, or electrical applications that require sensing or device complexity beyond what is possible in metallic electrodes. However, semiconductor NWs cannot be easily processed in such fashion due to the generally low malleability and higher melting points

in comparison to metals such as Ag and Au. For Si and many other semiconductors, the rapid formation of native oxide in the presence of air also produces high contact resistance between NWs [12]. This problem can be overcome by forming Si networks via top-down methods that pattern a network into a Si wafer [13], yet this strategy also precludes the advanced functionality (e.g. transistors [14], photovoltaic structures [15, 16], resistive memory elements [17], et al.) that can be encoded via bottom-up NW growth methods. Thus, the development of robust methods to facilitate electrically interconnected semiconductor NW networks that are flexible and transparent should lead to new application developments.

One strategy for inter-NW connectivity utilizes *in-situ* branching of the NWs. Branched semiconductor NW structures grown by a vapor-liquid-solid (VLS) mechanism can be generated through two or more VLS growth sequences with intervening catalyst deposition steps or through solution-seeded processes [18, 19]. Branched NWs have been shown to exhibit electrically-active junctions between the individual linear components [20, 21], and the sequential growth steps provide an opportunity to form homojunctions or heterojunctions at the branch points. Single-crystalline junctions have also been created between individual VLS-grown InSb and InAs NWs by precisely defining the growth position to yield intersections that can be electrically Ohmic [22–25]. In addition, flux

---

engineering has been used to create networks of VLS-grown indium tin oxide NWs [26]. Here, we build upon our previous report of a capillarity-driven welding mechanism in Si NWs by performing the welding process on centimeter-scale substrates containing tens of millions of NWs and characterizing the optical properties and electrical conductivity of the resulting mesh networks [27].

2   Results and discussion

As illustrated in Fig. 1, Si NWs were grown by a Au-catalyzed VLS process, collapsed with evaporating liquid N$_2$, and welded at temperatures between 815 and 875 °C, depending on diameter. This process generates a mesh of NWs with welded junctions at points of contact between NWs, as illustrated by the SEM images of a portion of a 6 cm^2 substrate shown in Fig. 1(c). Prior work verified that individual junctions exhibit Ohmic electrical transport characteristics with moderate junction resistance [27]. Here, we examine the diameter-dependent morphological characteristics and optical properties of the mesh films, and we report on the electrical transport through these networks both on rigid and flexible substrates.

The meshes are three-dimensional with the effective thickness of the network determined by both the density and diameter of the NWs. Plan-view SEM images of meshes composed of NWs nominally 20, 60, and 100 nm in diameter are shown in Fig. 2(a). Analysis of several regions of each sample before and after NW growth indicate that growth substrates for these samples exhibited Au catalyst and NW densities of ~ 80, ~ 3, and ~ 0.25 NWs/μm^2, respectively, values which result from differences in the density of Au nanoparticles in the initial colloidal solutions (7.0×10^{11}, 2.6×10^{10}, and 5.6×10^9 particles/mL, respectively). In addition, each sample shows a distribution of NW diameters, as shown by the histograms in Fig. 2(b), which are reasonably well fit to a Weibull distribution. Figure 2(c) illustrates the characteristic collapse height for NW mesh grown with these samples, which were found to be ~ 3, ~ 8, and 6–8 μm for the 20, 60, and 100 nm samples. Even though 20 nm networks have a NW density > 20 times higher than the 60 nm network, the average collapse height is nearly 3 times smaller. Similarly, the 60 nm sample has a density about ten-fold higher than 100 nm sample, yet it exhibits a similar collapse height. Thus, although density plays a role in the effective film height due to inter-NW interactions, NW diameter is a major predictor of the final height.

The trend in collapse height with diameter can be understood by considering the angle of deflection for a NW that experiences capillary forces during the collapse process. Assuming equal force distribution along the NW axis and modeling the NW

as a cantilever beam anchored at the base and undergoing deflection, we can qualitatively assess the diameter dependence of the collapse by calculating the angle of deflection, α, as [28]

$$\alpha = \frac{FL^3}{6EI} = \frac{64FL^3}{6\pi Ed^4} \tag{1}$$

where F is the average force acting on the NW perpendicular to the NW axis, L is the length of the NW, E is the Young's modulus of Si, and I is the moment of inertia, which can be related to diameter d by $I = \pi d^4/64$, yielding the expression on the right-hand side of Eq. (1). Because I increases rapidly with increasing NW diameter and is inversely proportional to α, the deflection angle decreases rapidly with increasing diameter. Thus, because of the reduced deflection, the effective collapse height increases for larger diameter NWs.

To create a large-area, flexible Si mesh, a sacrificial Ge layer was deposited on the Si/SiO$_2$ growth wafer prior to Au catalyst dispersal [29], as shown in the cross-sectional images in Fig. 3(a). This layer can be removed by wet-chemical etching in hydrogen peroxide, releasing the NW mesh from the substrate to create a free-standing film. However, due to difficulties in handling the lightweight networks, they were infiltrated with poly-dimethyl siloxane (PDMS) prior to Ge etching to provide additional handling stability, leading to the lift-off process illustrated in Fig. 3(b). As shown by photographs for NWs ~ 50 nm in diameter (Fig. 3(c)), the Ge layer can be etched to release a flexible, free-standing NW-PDMS film with good optical transparency. The color of the NW films depends strongly on the diameter of the constituent NWs. For instance, Fig. 4(a) displays photographs of a Si/SiO$_2$ growth wafer with NW meshes of nominal diameters of 15, 20, 30, 50, 60, and 100 nm. The apparent colors of the samples transition from blue to gray to brown as diameter increases. Optical transmission measurements on NW-PDMS films after release from the growth wafer are shown in Fig. 4(b) (solid lines) for nominal diameters of 20, 60, and 100 nm. The relative extinction of the samples increases at longer wavelengths as the diameter increases. These results are in good agreement with finite-element optical simulations of the transmittance spectra (dashed lines in Fig. 4(b)), which were calculated by weighting the simulated diameter-dependent spectra using the Weibull distributions shown in Fig. 2(b). The optical properties of the NW films strongly depend on diameter-dependent Lorentz-Mie resonances [30], and the results agree well with previous studies on the optical properties of disordered Si NW mats [31, 32].

To probe the electrical connectivity of the NW mesh over relatively large areas, we employed active voltage contrast imaging [33], which has been used to image electrical connectivity and percolation networks within silver NW networks [34],
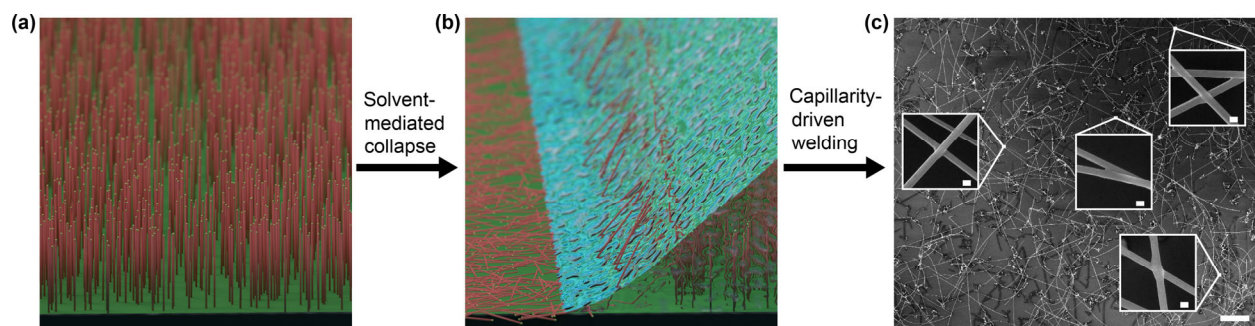

Figure 1   NW growth, collapse, and welding to form a mesh of interconnected NWs. (a) Schematic of initial VLS growth of Si NWs. (b) Schematic of NW collapse mediated by the capillary forces of evaporating liquid N$_2$. (c) SEM image of a collapsed NW mesh with interconnects welded by a capillarity-induced surface diffusion mechanism; scale bar, 10 μm. Insets: higher magnification SEM images of select welded NW junctions within the mesh; scale bars, 100 nm.
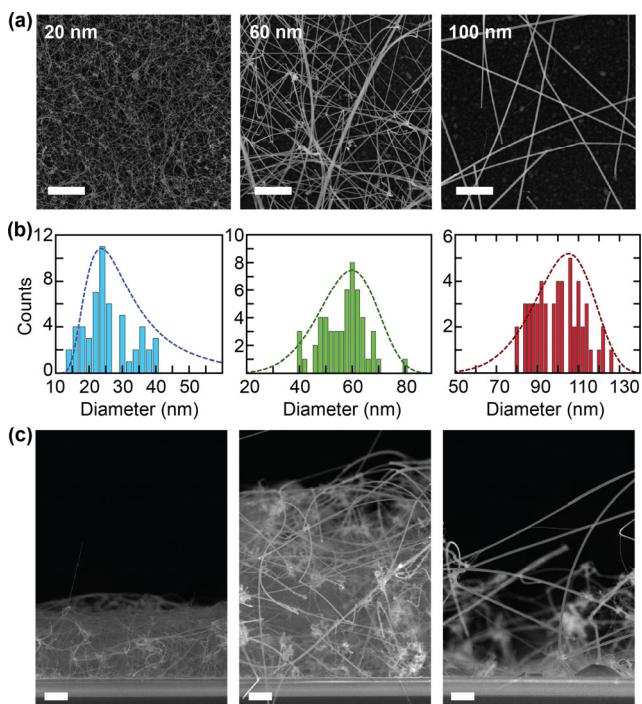
Figure 2 Diameter and density dependence of NW mesh height and morphology. (a) Top-down SEM images of collapsed and welded NWs grown with Au nanoparticles nominally 20 nm (left), 60 nm (middle) and 100 nm (right) in diameter; scale bars, 1 μm. (b) Histograms of NW diameter distributions for Au nanoparticle catalysts nominally 20 nm (left), 60 nm (middle) and 100 nm (right) in diameter. The best fit to a Weibull distribution is shown as the dashed line. (c) Cross-sectional SEM images of collapsed and welded NWs grown with Au nanoparticles nominally 20 nm (left), 60 nm (middle), and 100 nm (right) in diameter; scale bars, 1 μm.

to identify faults in integrated circuits [35], and to image the voltage threshold for metal NW junction formation via electroformation [36]. Voltage contrast imaging results from differences in the charging between electrically disconnected, floating structures and electrically connected (grounded or externally biased) structures. The contrast arises from secondary electrons that are deflected away from the detector due to the positive charging of structures. In other words, conductive pathways within the sample can be directly imaged (bright contrast) when the external electrical connection neutralizes the build-up of charge. The method can be implemented either with SEM or focused ion beam imaging, and Fig. 5 shows active voltage contrast images collected on various NW mesh

using the latter. Figure 5(a) displays a nearly 500 μm × 500 μm region with high contrast from NWs throughout the network. To confirm that these images indicate widespread electrical connectivity, a small square section of the network was electrically isolated using focused ion beam milling (Fig. 5(b)), eliminating the contrast within this section and confirming the electrical connectivity of the network. Comparison of standard SEM and active voltage contrast images indicate that more than 90% of the NWs on the substrate are electrically connected to one another.

To correlate the voltage contrast imaging with electrical conduction through a NW mesh, a small-scale network of NWs ~ 50 μm × 50 μm was fabricated, and four electrical contacts were defined, as shown by the SEM image in Fig. 5(c). Three of the electrodes contacted three separate sides of the network in dense (contacts 1 and 2) and sparse regions (contact 3), and the fourth electrode (contact 4) was electrically disconnected to serve as a floating reference during voltage contrast imaging. An active voltage contrast image of this network (Fig. 5(d)) with a bias of −20 V applied to contact 3 demonstrates electrical connection throughout most of the small-scale network with no contrast appearing from contact 4, as expected given its electrical isolation from the network. Current–voltage (*I*–*V*) curves were collected from each combination of contacts 1, 2, and 3, as shown in Fig. 5(e). The electrical resistance was determined to be ~ 85, ~ 4,200 and ~ 4,410 MΩ for contacts 1-2, 2-3, and 1-3, respectively. The ~ 50× lower resistance for contacts 1-2 can be attributed to substantially larger number of NWs that span the two contacts. In contrast, contact 3 is connected to the NW network by only a single NW; thus, the resistance between electrodes appears to be approximately inversely proportional to the number of NWs and electrical pathways connecting the electrodes. This result is in qualitative agreement with modeling of a percolating stick system [37], where the conductance, *σ*, can be expressed as

$$\sigma = \alpha \, (N - N_{\mathrm{C}})^{t} \qquad (2)$$

where *N* is the density of conducting sticks, N_{C} is the percolation threshold density, and *t* is a scaling exponent. Systems with electrical percolation often exhibit lower resistances at higher densities because of the increase in the number of parallel conduction pathways and significant decrease in the effective conduction path length [38]. Thus, as the NW density between electrodes increases, the conductance between the electrodes is expected to substantially increase [39].

To understand the electrical transport characteristics of centimeter-scale NW meshes on the growth substrate and
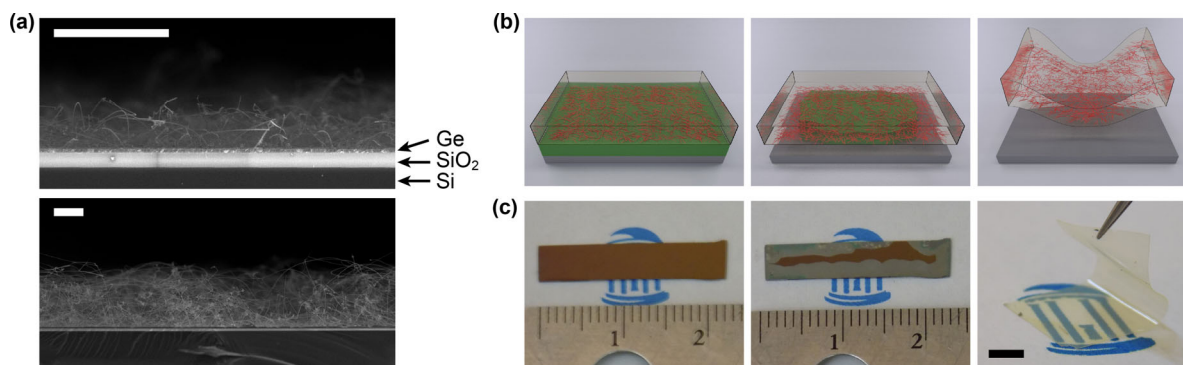

Figure 3 Lift-off of flexible Si NW mesh. (a) Cross-sectional SEM image of collapsed and welded NWs 30 nm (upper) and 60 nm (lower) in diameter. The Si substrates contain a 200 nm layer of Ge and 600 nm layer of SiO₂; scale bars, 5 μm. (b) Schematic of the lift-off process of PDMS-embedded mesh network, beginning with the mesh network embedded in PDMS (left), slow Ge underetch process (middle), and the resulting free-standing flexible network (right). (c) Photographs corresponding to the lift-off process illustrated in panel (b), resulting in a highly flexible PDMS-embedded NW network 5–15 μm thick; scale bar, 5 mm.
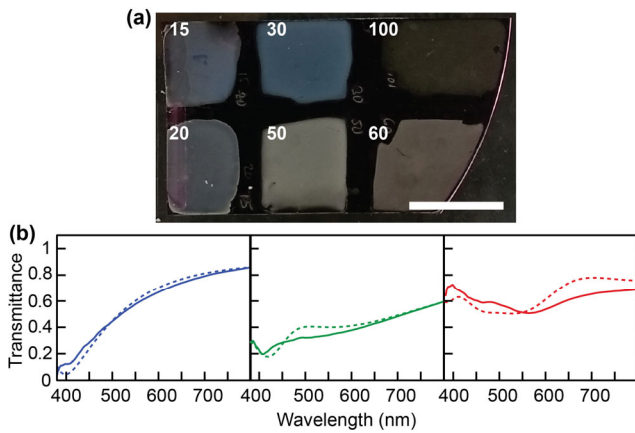
Figure 4 Diameter-dependent scattering and transmittance of meshes. (a) Photograph of a multi-section growth chip with NWs of various diameters; scale bar, 5 mm. (b) Simulated (dashed) and experimental (solid) transmittance data for 20, 60, and 100 nm NWs. Simulated transmittance was plotted using a weighted average determined from the magnitude of the Weibull distribution for each nominal diameter, and the simulated spectra are scaled to the maximum and minimum of the experimental spectra.

after lift-off from the growth substrate, meshes were fabricated on both a Si/SiO₂ substrate and Si/SiO₂/Ge substrate (for lift-off) using 50 nm diameter degenerately-doped n-type NWs with an encoded doping level of 2.5×10^{20} cm⁻³. Multiple macroscopic electrodes were fabricated on each NW mesh, as shown in Fig. 6(a). The results of electrical transport measurements across multiple contact configurations for both substrates are shown in Fig. 6(b), allowing the resistance of each mesh to be determined. The sheet resistances, as determined by the slope of the dashed lines in Fig. 6(b), are 170 ± 11 and 164 ± 29 kΩ/square for the on-substrate and substrate-free NW-PDMS films, respectively, showing no significant difference in resistance as a result of the lift-off process. The NW-PDMS device, however, exhibits a contact resistance of 39 ± 17 kΩ, which likely results from the decreased contact area between metal and NWs. The *I–V* curves of the films are linear over a broad voltage range (inset of Fig. 6(b)), demonstrating the high-quality of the Ohmic connections between the NWs. The performance of NW-PDMS films under strain was also probed by bending the film (inset of Fig. 6(c)). *I–V* data in Fig. 6(c) shows a less than 50% permanent increase in resistance under strain when measured across a 6 mm channel, demonstrating the
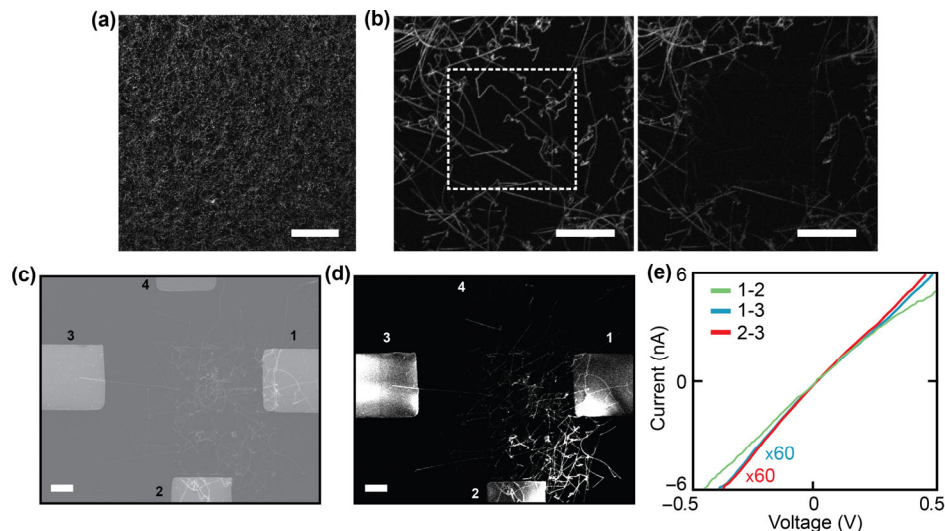

Figure 5 Visualizing electrical connectivity with voltage contrast imaging. (a) Active voltage contrast image collected by focused ion beam imaging using a −20 V bias to the NW mesh composed of 100 nm diameter NWs; scale bar, 100 μm. (b) Higher magnification active voltage contrast images before (left) and after (right) ion-beam milling of the perimeter of a square region (indicated by the dashed box in the left-hand image) to electrically disconnect the NWs inside the boxed region; scale bars, 10 μm. (c) Standard SEM image of a small area NW network of 100 nm diameter NWs with four electrical contacts to the network labeled 1–4; scale bar, 10 μm. (d) Active voltage contrast image by focused ion beam using a −20 V bias applied to electrode 3; scale bar, 10 μm. (e) Current–voltage measurements between electrodes 1-2 (green), 1-3 (blue), and 2-3 (red). Curves for 1-3 and 2-3 are scaled by a factor of 60.
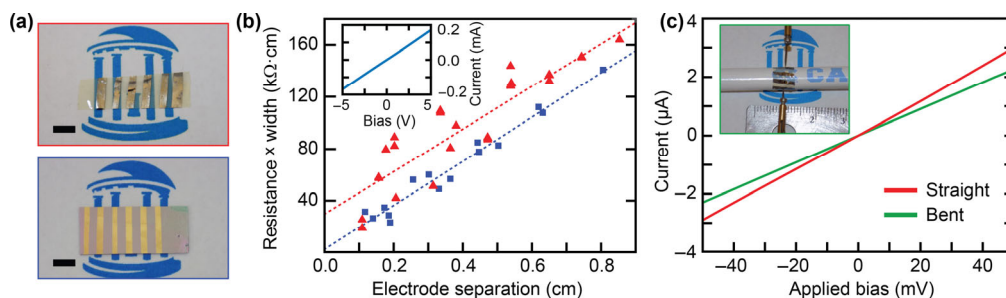

Figure 6 Electrical resistivity measurements on large-area, flexible Si NW mesh. (a) Photographs of PDMS-embedded network (top) and network on growth substrate (bottom) with deposited electrodes for *I–V* measurements; scale bars, 5 mm. (b) Resistance multiplied by channel width as a function of electrode separation (i.e. channel length) for ∼ 50 nm diameter NW networks measured on the Si growth substrate (blue squares) and on the substrate-free NW-PDMS film (red triangles). Dashed lines represent linear fits to the data, and the vertical offset of the dashed red line reflects a contact resistance of 39 ± 17 kΩ for the NW-PDMS film. Inset: *I–V* curve measured on the Si/SiO₂ growth substrate for an electrode separation of 1.5 mm. (c) *I–V* data for the NW-PDMS film when in a straight (red) and bent (green) conformation with a radius of curvature of ∼ 4 mm. Inset: photograph of the bent film contacted by electrical probe tips.

mechanical robustness of the electrical conductivity through the network. This behavior is consistent with flexibility observed in Ag NW networks [40].

3 Conclusions

We have demonstrated that capillarity-driven welding of Si NWs can be used to electrically interconnect NWs on a large scale to create flexible, conductive, and semi-transparent thin films composed of NW mesh. When released from growth substrates to produce free-standing, polymer-embedded films, the NW mesh exhibits minimal change in electrical resistance even when deformed to a small radius of curvature. The NW meshes are analogous to conductive networks created with metallic NW systems; however, the semiconducting nature of these NWs could lead to new applications as components in flexible/wearable electronics, as solar energy and battery electrodes [4], as bioelectronic sensing/signaling scaffolds [41, 42], and as a platform for neuromorphic computation using resistive memory elements [17, 43]. For instance, the volume density of junctions can easily meet or exceed 1 μm^{-3}, which is comparable to the density, $\sim 10^9$ mm^{-3}, of synapses in the human brain [44]. Although inherent disorder is often seen as an impediment to implementing semiconductor nanomaterials in realistic device applications, semiconductor NW meshes have promise for a variety of applications without the use of non-trivial lithography or assembly methods.

4 Methods

4.1 Synthesis of NWs and networks

A home-built chemical vapor deposition (CVD) system was used for all syntheses and includes a quartz-tube furnace (Lindberg Blue M), hydrogen (H_2) and argon (Ar) carrier gases (Matheson Trigas; 5N semiconductor grade), and reactive gases (Voltaix/Air Liquide Advanced Materials) silane (SiH_4), germane (GeH_4; 10% in H_2), and phosphine (PH_3; 1,000 ppm in H_2). NW growth substrates consisted of Si/SiO_2 wafers (Nova Electronic Materials; B-doped 1–10 $\Omega \cdot$cm Si wafers with 600 nm thermal oxide) and were optionally coated with a $\sim$ 200 nm sacrificial Ge layer following a modified literature procedure [29]. Briefly, substrates were annealed for 10 min at 600 °C with 100 standard cubic centimeters per minute (sccm) of H_2, a seed layer was deposited for 1 min at 350 °C and 20 Torr using 1 sccm SiH_4 and 10 sccm B_2H_6 with 60 sccm Ar, and Ge was deposited for 75 min at 330 °C and 5 Torr using 10 sccm of GeH_4 and 100 sccm H_2. The Si/SiO_2 or Si/SiO_2/Ge substrates were then placed in an ultraviolet/ozone cleaner (Samco UV-1) and functionalized with a 10:1 water: poly-L-lysine (0.1% in H_2O, Sigma Aldrich) solution followed by dispersion of citrate-stabilized Au colloids (BBI international) with diameters of 20–100 nm. N-type Si NWs were grown in the CVD system following a modified literature procedure using a 5-min 450 °C nucleation step followed by a ramp (1 °C/min cooling rate) to 420 °C with 200 sccm H_2, 2 sccm SiH_4, 10 sccm PH_3, and a total growth time of 5 h at a pressure of 20 Torr [27, 45]. This growth condition yields a diameter independent growth rate of $\sim$ 200 nm/min, yielding NWs $\sim$ 60 μm in length across all samples [45]. Elemental analysis by energy dispersive X-ray spectroscopy (not shown) indicates that a small fraction of Ge (< 1 atomic%) can be incorporated in the NWs likely due to sublimation and/or diffusion of Ge from the substrate. Note that we have found that a 10–50 nm layer of SiO_x deposited on top of the Ge layer (not shown) by plasma enhanced chemical vapor deposition (Advanced Vacuum Vision 310) prior to Au

colloid dispersal can prevent Ge participation in NW growth. NW arrays were collapsed by pressuring the quartz tube to one atmosphere of Ar using a continuous flow of 200 sccm Ar, disconnecting the quartz tube at the downstream end (while continuing Ar flow, with the remaining upstream end connected to a flexible braided stainless steel vacuum hose), placing the open end of the quartz tube in a dewar flask of liquid nitrogen, and sliding the NW growth chip (by gently tapping on the tube) into the liquid nitrogen, where it remained for $\sim$ 30 s. The substrate was then quickly removed from the liquid nitrogen and placed at the end of the quartz tube using tweezers (with continuing Ar flow), reinserted into the center of the quartz tube using a quartz rod, and evacuated to vacuum. Evaporation of liquid nitrogen caused collapse of the NWs without formation of an oxide layer. The welding process was performed by raising the temperature to 800–900 °C under 200 sccm H_2 at 8 Torr. At the desired temperature, the H_2 flow was reduced to 60 sccm, the pressure was ramped to 25 Torr, the conditions were held for 4 min, and the system was then cooled to room temperature.

4.2 Electron microscopy imaging

SEM imaging, ion-beam imaging, and ion-beam milling was performed using an FEI Helios 600 Nanolab Dual Beam system using a Ga source.

4.3 Flexible network fabrication

For fabrication of NW-PDMS films, Si/SiO_2/Ge substrates were used for NW growth, and PDMS (Sylgard 184 Silicone Elastomer) was spun cast onto the NW networks (500 rpm for 5 s and 1,500 rpm for 30 s). The substrates were cured for 60 min at 60 °C. Polymer was removed from the edges of the substrate, and the substrate was immersed in 30% hydrogen peroxide at 80 °C for several days to remove the Ge layer.

4.4 Transport measurements

For measurements on NW networks, titanium/palladium (Ti/Pd) contacts (5/200 nm) were evaporated, after a brief oxide etch in a buffered hydrogen fluoride (BHF) solution, onto the exposed NW networks via a shadow mask in an electron beam evaporator (Thermionics VE-100). For single-junction measurements, welded NWs were mechanically transferred onto device substrates (Nova Electronic Materials; B-doped 1–10 $\Omega \cdot$cm Si wafers with 100 nm thermal oxide and 200 nm silicon nitride). Electron-beam lithography was used to pattern electrical contacts to individual NWs, and Ti/Pd contacts (3/200 nm) were evaporated after a brief etch in BHF. I–V data for both NW networks and single welded junctions were collected with a Keithley 2636A SourceMeter in conjunction with Signatone micropositioners (S-725) and probe tips (SE-TL) or a Lake Shore Cryotronics PS-100 probe station. NW diameters and channel lengths were measured by SEM. For measurements in a bent configuration, NW-PDMS films were wrapped around a pencil to demonstrate the durability of the networks.

4.5 Absorbance data

Junction transmittance spectra were measured with a microspectrophotometer (20/30 PV UV-Visible-NIR from Craic Industries) using a 10× objective (Ultrafluor 10x 0.2 NA 7.4 mm WD) in conjunction with a Xe arc lamp source and CCD array detector. Optical simulations were performed using COMSOL Multiphysics. The two-dimensional simulation domain consisted of a Si NW with a circular cross-section placed in a vacuum encapsulated by perfectly matched layers

(PMLs) to prevent reflection/scattering effects from the simulation boundaries. Absorption characteristics of single NWs were simulated by impinging a plane wave with either transverse electric (TE) or transverse-magnetic (TM) polarization using the total-field, scattered-field method. A polarization-independent transmittance was calculated by averaging the TE and TM transmittance. The simulation was repeated for NW diameters from 20 to 145 nm in steps of 3 nm.

Notes

The authors declare no competing financial interest.

References

[1]   Lieber, C. M. Semiconductor nanowires: A platform for nanoscience and nanotechnology. *MRS Bull.* **2011**, *36*, 1052–1063.

[2]   Zhang, A. Q.; Zheng, G. F.; Lieber, C. M. *Nanowires: Building Blocks for Nanoscience and Nanotechnology*; Springer: Cham, 2016.

[3]   Tian, B. Z.; Cohen-Karni, T.; Qing, Q.; Duan, X. J.; Xie, P.; Lieber, C. M. Three-dimensional, flexible nanoscale field-effect transistors as localized bioprobes. *Science* **2010**, *329*, 830–834.

[4]   Chan, C. K.; Peng, H. L.; Liu, G.; McIlwrath, K.; Zhang, X. F.; Huggins, R. A.; Cui, Y. High-performance lithium battery anodes using silicon nanowires. *Nat. Nanotechnol.* **2008**, *3*, 31–35.

[5]   Takei, K.; Takahashi, T.; Ho, J. C.; Ko, H.; Gillies, A. G.; Leu, P. W.; Fearing, R. S.; Javey, A. Nanowire active-matrix circuitry for low-voltage macroscale artificial skin. *Nat. Mater.* **2010**, *9*, 821–826.

[6]   Garg, R.; Rastogi, S. K.; Lamparski, M.; de la Barrera, S. C.; Pace, G. T.; Nuhfer, N. T.; Hunt, B. M.; Meunier, V.; Cohen-Karni, T. Nanowire-mesh-templated growth of out-of-plane three-dimensional fuzzy graphene. *ACS Nano* **2017**, *11*, 6301–6311.

[7]   Sandler, J. K. W.; Kirk, J. E.; Kinloch, I. A.; Shaffer, M. S. P.; Windle, A. H. Ultra-low electrical percolation threshold in carbon-nanotube-epoxy composites. *Polymer* **2003**, *44*, 5893–5899.

[8]   De, S.; Higgins, T. M.; Lyons, P. E.; Doherty, E. M.; Nirmalraj, P. N.; Blau, W. J.; Boland, J. J.; Coleman, J. N. Silver nanowire networks as flexible, transparent, conducting films: Extremely high DC to optical conductivity ratios. *ACS Nano* **2009**, *3*, 1767–1774.

[9]   Hu, L. B.; Kim, H. S.; Lee, J. Y.; Peumans, P.; Cui, Y. Scalable coating and properties of transparent, flexible, silver nanowire electrodes. *ACS Nano* **2010**, *4*, 2955–2963.

[10]   Lyons, P. E.; De, S.; Elias, J.; Schamel, M.; Philippe, L.; Bellew, A. T.; Boland, J. J.; Coleman, J. N. High-performance transparent conductors from networks of gold nanowires. *J. Phys. Chem. Lett.* **2011**, *2*, 3058–3062.

[11]   Rathmell, A. R.; Wiley, B. J. The synthesis and coating of long, thin copper nanowires to make flexible, transparent conducting films on plastic substrates. *Adv. Mater.* **2011**, *23*, 4798–4803.

[12]   Rabbani, M. G.; Patil, S. R.; Verma, A.; Villarreal, J. E.; Korgel, B. A.; Nekovei, R.; Khader, M. M.; Darling, R. B.; Anantram, M. P. Zero-bias photocurrents in highly-disordered networks of Ge and Si nanowires. *Nanotechnology* **2016**, *27*, 045201.

[13]   Hossain, M.; Kumar, G. S.; Barimar Prabhava, S. N.; Sheerin, E. D.; McCloskey, D.; Acharya, S.; Rao, K. D. M.; Boland, J. J. Transparent,

[14]   Cui, Y.; Wei, Q. Q.; Park, H.; Lieber, C. M. Nanowire nanosensors for highly sensitive and selective detection of biological and chemical species. *Science* **2001**, *293*, 1289–1292.

[15]   Kempa, T. J.; Tian, B. Z.; Kim, D. R.; Hu, J. S.; Zheng, X. L.; Lieber, C. M. Single and tandem axial *p-i-n* nanowire photovoltaic devices. *Nano Lett.* **2008**, *8*, 3456–3460.

[16]   Hill, D. J.; Teitsworth, T. S.; Ritchie, E. T.; Atkin, J. M.; Cahoon, J. F. Interplay of surface recombination and diode geometry for the performance of axial p–i–n nanowire solar cells. *ACS Nano* **2018**, *12*, 10554–10563.

[17]   Christesen, J. D.; Pinion, C. W.; Grumstrup, E. M.; Papanikolas, J. M.; Cahoon, J. F. Synthetically encoding 10 nm morphology in silicon nanowires. *Nano Lett.* **2013**, *13*, 6281–6286.

[18]   Wang, D. L.; Qian, F.; Yang, C.; Zhong, Z. H.; Lieber, C. M. Rational growth of branched and hyperbranched nanowire structures. *Nano Lett.* **2004**, *4*, 871–874.

[19]   Grebinski, J. W.; Hull, K. L.; Zhang, J.; Kosel, T. H.; Kuno, M. Solution-based straight and branched CdSe nanowires. *Chem. Mater.* **2004**, *16*, 5260–5272.

[20]   Zhu, J.; Peng, H. L.; Chan, C. K.; Jarausch, K.; Zhang, X. F.; Cui, Y. Hyperbranched lead selenide nanowire networks. *Nano Lett.* **2007**, *7*, 1095–1099.

[21]   Jiang, X. C.; Tian, B. Z.; Xiang, J.; Qian, F.; Zheng, G. F.; Wang, H. T.; Mai, L. Q.; Lieber, C. M. Rational growth of branched nanowire heterostructures with synthetically encoded properties and function. *Proc. Natl. Acad. Sci. USA* **2011**, *108*, 12212–12216.

[22]   Plissard, S. R.; van Weperen, I.; Car, D.; Verheijen, M. A.; Immink, G. W. G.; Kammhuber, J.; Cornelissen, L. J.; Szombati, D. B.; Geresdi, A.; Frolov, S. M. et al. Formation and electronic properties of InSb nanocrosses. *Nat. Nanotechnol.* **2013**, *8*, 859–864.

[23]   Car, D.; Wang, J.; Verheijen, M. A.; Bakkers, E. P. A. M.; Plissard, S. R. Rationally designed single-crystalline nanowire networks. *Adv. Mater.* **2014**, *26*, 4875–4879.

[24]   Dalacu, D.; Kam, A.; Austing, D. G.; Poole, P. J. Droplet dynamics in controlled InAs nanowire interconnections. *Nano Lett.* **2013**, *13*, 2676–2681.

[25]   Rieger, T.; Rosenbach, D.; Vakulov, D.; Heedt, S.; Schäpers, T.; Grützmacher, D.; Lepsa, M. I. Crystal phase transformation in self-assembled InAs nanowire junctions on patterned Si substrates. *Nano Lett.* **2016**, *16*, 1933–1941.

[26]   Beaudry, A. L.; LaForge, J. M.; Tucker, R. T.; Sorge, J. B.; Adamski, N. L.; Li, P.; Taschuk, M. T.; Brett, M. J. Directed branch growth in aligned nanowire arrays. *Nano Lett.* **2014**, *14*, 1797–1803.

[27]   Celano, T. A.; Hill, D. J.; Zhang, X.; Pinion, C. W.; Christesen, J. D.; Flynn, C. J.; McBride, J. R.; Cahoon, J. F. Capillarity-driven welding of semiconductor nanowires for crystalline and electrically ohmic junctions. *Nano Lett.* **2016**, *16*, 5241–5246.

[28]   Gere, J. M.; Timoshenko, S. P. *Mechanics of Materials*, 4th ed.; PWS Publish Company: Boston, 1997.

[29]   Tada, M.; Park, J. H.; Kuzum, D.; Thareja, G.; Jain, J. R.; Nishi, Y.; Saraswat, K. C. Low temperature germanium growth on silicon oxide using boron seed layer and *in situ* dopant activation. *J. Electrochem. Soc.* **2010**, *157*, H371–H376.

[30]   Cao, L. Y.; Fan, P. Y.; Barnard, E. S.; Brown, A. M.; Brongersma, M. L. Tuning the color of silicon nanostructures. *Nano Lett.* **2010**, *10*, 2649–2654.

[31]   Bao, H.; Zhang, W. X.; Chen, L. L.; Huang, H. X.; Yang, C.; Ruan, X. L. An investigation of the optical properties of disordered silicon nanowire mats. *J. Appl. Phys.* **2012**, *112*, 124301.

[32]   Holmberg, V. C.; Bogart, T. D.; Chockla, A. M.; Hessel, C. M.; Korgel, B. A. Optical properties of silicon and germanium nanowire fabric. *J. Phys. Chem. C* **2012**, *116*, 22486–22491.

[33]   Rosenkranz, R. Failure localization with active and passive voltage contrast in FIB and SEM. *J. Mater. Sci.: Mater. Electron.* **2011**, *22*, 1523–1535.

[34]   Fairfield, J. A.; Ritter, C.; Bellew, A. T.; McCarthy, E. K.; Ferreira, M. S.; Boland, J. J. Effective electrode length enhances electrical activation of nanowire networks: Experiment and simulation. *ACS Nano* **2014**, *8*, 9542–9549.

[35] Sabate, A. C.; Ismail, N.; Nordin, N. Innovative way of implementing active voltage contrast. In *Proceedings of the 20th IEEE International Symposium on the Physical and Failure Analysis of Integrated Circuits*, Suzhou, China, 2013, pp 132–135.

[36] Nirmalraj, P. N.; Bellew, A. T.; Bell, A. P.; Fairfield, J. A.; McCarthy, E. K.; O'Kelly, C.; Pereira, L. F. C.; Sorel, S.; Morosan, D.; Coleman, J. N. et al. Manipulating connectivity and electrical conductivity in metallic nanowire networks. *Nano Lett*. **2012**, *12*, 5966–5971.

[37] De, S.; King, P. J.; Lyons, P. E.; Khan, U.; Coleman, J. N. Size effects and the problem with percolation in nanostructured transparent conductors. *ACS Nano* **2010**, *4*, 7064–7072.

[38] Balberg, I.; Binenbaum, N. Computer study of the percolation threshold in a two-dimensional anisotropic system of conducting sticks. *Phys. Rev. B* **1983**, *28*, 3799–3812.

[39] Hu, L.; Hecht, D. S.; Grüner, G. Percolation in transparent and conducting carbon nanotube networks. *Nano Lett*. **2004**, *4*, 2513–2517.

[40] Yang, L. Q.; Zhang, T.; Zhou, H. X.; Price, S. C.; Wiley, B. J.; You, W. Solution-processed flexible polymer solar cells with silver nanowire electrodes. *ACS Appl. Mater. Interfaces* **2011**, *3*, 4075–4084.

[41] Xie, C.; Liu, J.; Fu, T. M.; Dai, X. C.; Zhou, W.; Lieber, C. M. Three-dimensional macroporous nanoelectronic networks as minimally invasive brain probes. *Nat. Mater*. **2015**, *14*, 1286–1292.

[42] Acarón Ledesma, H.; Li, X. J.; Carvalho-de-Souza, J. L.; Wei, W.; Bezanilla, F.; Tian, B. Z. An atlas of nano-enabled neural interfaces. *Nat. Nanotechnol*. **2019**, *14*, 645–657.

[43] Thomas, A. Memristor-based neural networks. *J. Phys. D*: *Appl. Phys*. **2013**, *46*, 093001.

[44] DeFelipe, J.; Marco, P.; Busturia, I.; Merchán-Pérez, A. Estimation of the number of synapses in the cerebral cortex: Methodological considerations. *Cereb. Cortex* **1999**, *9*, 722–732.

[45] Pinion, C. W.; Nenon, D. P.; Christesen, J. D.; Cahoon, J. F. Identifying crystallization- and incorporation-limited regimes during vapor–liquid–solid growth of Si nanowires. *ACS Nano* **2014**, *8*, 6081–6088.